ADVANCES IN ATMOSPHERIC SCIENCES, VOL. 39, DECEMBER 2022, 2056–2070

• **Original Paper** •

The Microphysical Characteristics of Wintertime Cold Clouds in North China※

Xuexu WU[1,2], Minghuai WANG[*1,2], Delong ZHAO[*1,3], Daniel ROSENFELD[1,4], Yannian ZHU[1,2], Yuanmou DU[3], Wei ZHOU[3], Ping TIAN[3], Jiujiang SHENG[3], Fei WANG[3], and Deping DING[3]

[1]*School of Atmospheric Sciences, Nanjing University, Nanjing* 210023, *China*

[2]*Joint International Research Laboratory of Atmospheric and Earth System Sciences & Institute for Climate and Global Change Research, Nanjing University, Nanjing* 210023, *China*

[3]*Beijing Weather Modification Office, Beijing* 100089, *China*

[4]*Institute of Earth Sciences, The Hebrew University of Jerusalem, Jerusalem* 91904, *Israel*

(Received 15 July 2021; revised 2 March 2022; accepted 28 March 2022)

ABSTRACT

The microphysical characteristics of wintertime cold clouds in North China were investigated from 22 aircraft observation flights from 2014 to 2017, 2020, and 2021. The clouds were generated by mesoscale weather systems with little orographic component. Over the mixed-phase temperature range (–40°C to 0°C), the average fraction of liquid, mixed-phase, and ice cloud was 4.9%, 23.3%, and 71.8%, respectively, and the probability distribution of ice mass fraction was a half-U-shape, suggesting that ice cloud was the primary cloud type. The wintertime mixed-phase clouds in North China were characterized by large cloud droplet number concentration, small liquid water content (LWC), and small effective diameter of cloud droplets. The main reason for larger cloud droplet number concentration and smaller effective diameter of cloud droplets was the heavy pollution in winter in North China, while for smaller LWC was the lower temperature during flights and the difference in air mass type. With the temperature increasing, cloud droplet number concentration, LWC, and the size of ice particles increased, but ice number concentration and effective diameter of cloud droplets decreased, similar to other mid-latitude regions, indicating the similarity in the temperature dependence of cloud properties of mixed-phase clouds. The variation of the cloud properties and ice habit at different temperatures indicated the operation of the aggregation and riming processes, which were commonly present in the wintertime mixed-phase clouds. This study fills a gap in the aircraft observation of wintertime cold clouds in North China.

Key words: cold clouds, aircraft observation, microphysical character, North China

Citation: Wu, X. X., and Coauthors, 2022: The microphysical characteristics of wintertime cold clouds in North China. *Adv. Atmos. Sci.*, **39**(12), 2056−2070, https://doi.org/10.1007/s00376-022-1274-4.

Article Highlights:

- Ice clouds were the primary cloud type in winter in North China, while the proportions of mixed-phase and supercooled clouds were small.
- The temperature dependence of cloud properties for wintertime mixed-phase clouds was similar to other mid-latitude regions.
- The aggregation and riming processes were commonly presented in the wintertime mixed-phase clouds.

1. Introduction

Cold clouds, where water vapor, supercooled liquid droplets, and ice crystals could coexist, are common from the polar regions to the tropics (Hu et al., 2010; Korolev et al., 2017; Storelvmo, 2017). Due to the difference in water saturation vapor pressure between ice and supercooled water, cold clouds are in a thermodynamically unstable state (Korolev, 2007a). As a result, in cold clouds, the hydrometeors (e.g., supercooled cloud droplets, ice crystals, graupel, snowflake, even hailstone) vary in quantity and type, and the microphysical processes are complex (Korolev et al., 2017; Morrison et al., 2020). As such, cold clouds play an

※ This paper is a contribution to the special issue on Cloud–Aerosol–Radiation–Precipitation Interaction: Progress and Challenges.

* Corresponding authors: Minghuai WANG, Delong ZHAO
Emails: minghuai.wang@nju.edu.cn, zhaodelong@bj.cma.gov.cn

important but complex role in modulating the life cycle of clouds, the formation of precipitation, and the radiative energy budget of the earth. Thus, the observation of cold clouds is critical for understanding these processes better.

Aircraft is the most direct method for measuring cold clouds due to its high temporal and spatial resolution compared to remote sensing methods (Noh et al., 2011; Ahn et al., 2018). The microphysical characters of cold clouds have been obtained directly in different regions around the world by aircraft (Plummer et al., 2014; Young et al., 2016; Ahn et al., 2017; Lloyd et al., 2018; Huang et al., 2021), providing a better understanding of the microphysical structure, the optical characteristics, and the microphysical processes of cold clouds. Using the aircraft observation data in North America, Gultepe et al. (2002) found that both the cloud droplet number concentration (N_c) and liquid water content (LWC) decreased with temperature decreasing, and N_c and LWC varied over a considerable range within the same temperature interval. Taylor et al. (2016) presented aircraft observations of the microphysical characters of cold clouds in the UK from the COPE campaign. They outlined the importance of the freezing and riming process in the ice formation in mixed-phase clouds. Wang et al. (2020) investigated the microphysical properties of cold clouds in generating cells over the Southern Ocean during the SOCRATES campaign. The results suggested that N_c, LWC, and ice particle number concentration (N_i) inside the generating cells were larger than those between generating cells, indicating the significant spatial heterogeneity in cold clouds. What's more, the observation results of cold clouds from aircraft were also used to evaluate and improve satellite retrieval algorithms (Noh et al., 2011; Ahn et al., 2018) and microphysics schemes in model simulation (Gultepe and Isaac, 2004).

Aircraft observations of cold clouds have been carried out in recent years over China (Guo et al., 2015; Quan and Jia, 2020), but the observations in winter are rare. The existing studies have been mainly in the warm season, and their analysis usually focused on just one flight. Zhao and Lei (2014) described the vertical profiles of cloud properties from the aircraft observation of a cold cloud case in spring in Henan Province, and they found an inverse relationship between N_c and N_i. Zhu et al. (2015) investigated the ice habit and ice growth processes in stratiform clouds with embedded convection in Hebei Province. The results suggested that the dominant ice growth process differed between shallow stratiform clouds and embedded convection. From the analysis of the microphysical properties of the cold clouds in North China in spring, Yang and Lei (2016) found that the ice particles grew during falling via the riming and aggregation processes within precipitating area. Although some observations for wintertime cold clouds have been achieved by radar or other methods (Huo et al., 2020), the lack of aircraft observation still severely limited our understanding of them.

To broaden the knowledge of wintertime cold clouds in North China, we used the aircraft observational data from Beijing Weather Modification Office (BJWMO). The data was collected by BJWMO from a series of observations around Beijing since 2014 (Ma et al., 2017) by aircraft and several surface measurements. The aircraft flight routes were planned based on short-term predictions of clouds associated with mesoscale weather systems. The multi-source observation datasets for wintertime clouds have been obtained in North China from these measurements, which will help us better understand these clouds. This study aims to fill the gaps in the observations of mixed-phase clouds in North China and determine the similarities and differences of wintertime mixed-phase clouds between different mid-latitude regions, such as North America, East Europe, and the Southern Ocean.

This paper is organized as follows: Section 2 introduces the dataset, the aircraft measurements, and methods of data processing used in this study. Section 3 describes the results, including the statistics of cloud microphysical properties, the temperature dependence of cloud microphysical properties, the particle size distributions (PSDs), the ice habits, and the microphysical processes at different temperatures. The summary is given in section 4.

2. Data and method

2.1. *Overview of the flights*

The observation data used in this study were provided by the King Air 350 research aircraft from BJWMO. The data were collected during the winters of 2014 to 2017 and 2020 to 2021, and 22 flights with in-cloud samples in the mixed-phase temperature range (MPTR, −40°C to 0°C) were selected. These flights aimed to observe the cloud microphysical characters and/or cloud-seeding around Beijing after receiving forecasts of rain or snow, although the sampled clouds had little orographic component. Cloud seeding has been shown to be effective in winter mixed-phase orographic clouds (French et al., 2018; Friedrich et al., 2020), but investigating such clouds was not the present study's focus. In the cloud seeding flights, after the end of observations, the cloud seeding was carried out, and the aircraft flew out of the region after seeding. Therefore, the possible influence of cloud seeding could not be observed by aircraft, meaning the observation could represent the naturally occurring clouds.

The main area of these flights was in the northwest part of Beijing, located in the transition region between the North China Plain and Yanshan Mountain (Fig. 1). The primary cloud type for wintertime clouds in this area was stratiform clouds. The tracks of these flights are shown in Fig. 1 as well. The track was predefined before each observation flight, adjustable according to the weather condition or the air control during the flight. The aircraft sampled clouds during the flight without being specially selected, except for some convective clouds with strong vertical motion. The aircraft did not avoid the area with suspected freezing rain or large supercooled drops during the flight. The aircraft

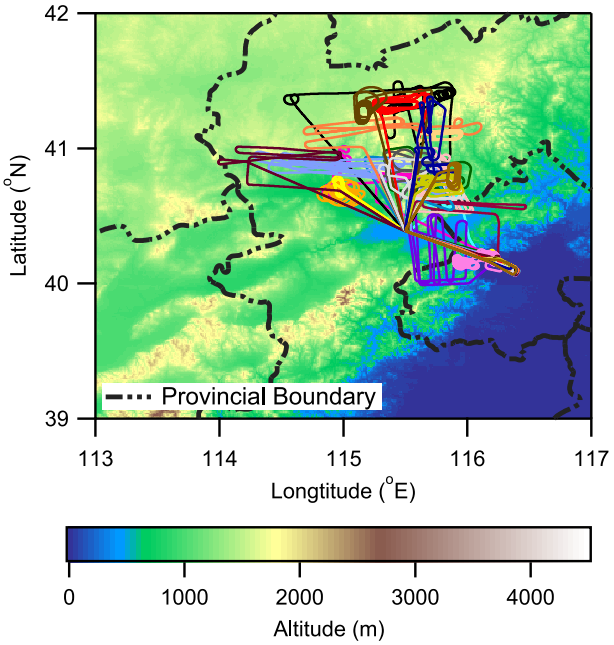

Fig. 1. The topography of the observation area (contour map) and the tracks of the observation flights (colored lines). Different colors represent different flights.

crossed the target clouds horizontally during sampling, and the sampling mostly occurred in the middle of the clouds. The highest altitude during these flights was about 7500 m above sea level (ASL), while most of the flights were lower than 4000 m ASL.

2.2. *Aircraft measurements*

To obtain the meteorological, aerosol, and cloud properties in real-time during the flight, a series of in situ instruments were equipped in the King Air 350 aircraft. The primary airborne probes used in this study are the Aircraft Integrated Meteorological Measurement System 20 (Aventech Research Inc. Ontario, Canada), the Fast Cloud Droplet Probe (Stratton Park Engineering Company (SPEC) Inc. Boulder, USA), and the Two-Dimensional Stereo Optic Array Spectrometer (SPEC). The staff of BJWMO periodically calibrated the airborne probes in the laboratory and before each flight.

The Aircraft Integrated Meteorological Measurement System 20 (AIMMS-20) is designed to deliver high-frequency real-time meteorological data during the flight, including three-dimensional wind, temperature, pressure, true airspeed. In addition, the aircraft flight information (longitude, latitude, and altitude) and high-precision aircraft attitude data (bank angle, pitch angle, and true heading) are provided by AIMMS-20.

The Fast Cloud Droplet Probe (FCDP), which utilizes forward scattering to detect particles, measures N_c and the cloud PSD from 2 to 50 μm. The range of the FCDP is divided into 20 different bins, and the resolution of FCDP (the width of the bin) changes from 1.5 μm to 4 μm for different bins with the diameter of particles increasing. To reduce the error caused by the shattering of ice, anti-shattering tips were equipped on FCDP (Korolev et al., 2011). In our study, the mass concentration of FCDP (M_{FCDP}) was calculated from the cloud PSD using the formula (1), assuming that all particles were spherical water droplets:

$$M = \int_{D_{\min}}^{D_{\max}} \frac{1}{6}\pi D^3 \rho_w n(D)\mathrm{d}D\,, \tag{1}$$

where D is the diameter of the particle, ρ_w is the density of water, and $n(D)$ is the particle size distribution.

The Two-Dimensional Stereo Optic Array Spectrometer (2DS) is a widely used optical array probe (OAP) with high spatial and temporal resolution in cloud microphysical research. Consisting of two orthogonal 128-photodiode arrays, 2DS can provide 10μm resolution shadow images of the large cloud droplets, ice, and precipitation particles over the range from 10 μm to 1280 μm (Lawson et al., 2006b). In our study, 2DS was equipped with anti-shattering tips as well. The number concentration and PSDs from 2DS could be determined from these shadow images using the data processing methods for OAPs. The techniques of data processing used in our study are introduced in section 2.3.

2.3. *Data processing*

Since the time resolution of AIMMS-20, FCDP, and 2DS were different, the data of all probes were averaged to 1-second intervals for further analysis. During the observation, the airspeed was about 100 m s^{-1}. Therefore, this time resolution was equivalent to a spatial resolution of about 100 m in our study.

To get the information from 2DS, including particle number concentration, PSDs, LWC, ice water content (IWC), and other information, we needed to analyze the shadow images taken by 2DS. There have been many approaches to OAP image data processing; we used the method proposed by Crosier et al. (2011) in this study. To minimize possible errors, the following corrections were used when processing 2DS data: (1) the method of Korolev (2007b) was employed to reconstruct the "out of focus" particles due to diffraction to get their real size; (2) particles with interarrival times (IAT) smaller than 10^{-6} s (Taylor et al., 2016) were rejected to remove the shattered artifacts; (3) the "center-in" formula (Heymsfield and Parrish, 1978) was used to calculate the sample volume; and (4) we only considered particles having centers within the photodiode array.

After these corrections, we classified the particles from 2DS by their difference in shape. In order to better distinguish different particles from 2DS, we used the definition of the circularity value (C) of each particle from formula (2) as Crosier et al. (2011):

$$C = \frac{P^2}{4\pi A}\,, \tag{2}$$

where P is the particle perimeter, and A is the particle area.

According to the isoperimetric inequality, the circularity value of a circle equals 1. For other shapes, the circularity value is greater than 1. The closer the geometric shape is to a circle, the closer the circularity value is to 1. However, due to the limited resolution of 2DS, particles containing < 20 pixels (equal to about 50 μm) could not be classified in this method since they contained insufficient pixels to determine the shape accurately. Besides, the number concentration can be overestimated by 2DS in the smaller bins, so we needed to omit the first 1–5 bins of 2DS (10 to 50 μm) (Jackson et al., 2012; Jensen et al., 2013). Therefore, we could only distinguish the ice particles and liquid droplets larger than 50 μm from 2DS.

As a result of the differences in shape between liquid droplets and ice particles (Lawson et al., 2006a; Crosier et al., 2011), in our study, particles with $C < 1.2$ were indicative of liquid droplets, while particles with $C > 1.2$ were associated with ice particles. Previous studies (Taylor et al., 2016; O'Shea et al., 2017) have suggested that the threshold of circularity value in our study was reasonable to distinguish between ice particles and liquid droplets. Under most conditions, this classification was suitable, but the round ice particles might be misclassified in pure ice clouds. To remove this potential misclassification, we used FCDP and AIMMS-20 to define the in-cloud sample as pure ice cloud when temperature < –40°C or $N_{FCDP} \leqslant 1$ cm^{-3}.

Due to the lack of a bulk water probe (e.g., Hotwire water content probe), we calculated the LWC and IWC from the PSDs after the phase determination. The LWC of 2DS (LWC_{2DS}) and FCDP (LWC_{FCDP}) were calculated from the 2DS liquid PSDs and FCDP PSDs using formula (1). Faber et al. (2018) compared LWC between the CDP and a Nevzorov hotwire probe, and they found that the CDP-estimated LWC exceeded that measured by the hotwire probe by approximately 20%. Figure A1 compares the Hotwire LWC ($LWC_{Hotwire}$) to the estimated LWC (LWC_{est}) on the King Air 350 aircraft, as conducted by the staff of BJWMO in their laboratory. The linear best fit line was $LWC_{Hotwire} = 0.74LWC_{est} + 0.004$ with a correlation coefficient of 0.88. Unlike LWC, IWC was estimated in the form $m = aD^b$, where D is the diameter of the ice particle from the shadow images and a and b are empirically derived parameters. Previous studies have proposed several different sets of parameters a and b (Brown and Francis, 1995; Baker and Lawson, 2006; Heymsfield et al., 2010; Korolev et al., 2013; Wang et al., 2015). IWC as measured by Hotwire have been found to be nearly the same as the PSD estimation for $D < 4$ mm (Korolev et al., 2013). In comparison, the relationship from Heymsfield et al. (2010, hereafter H10) came from more recent airborne observations with broader temperatures ranging from 0°C to –60°C, and particle sizes between 100 and 2000 μm. Therefore, we estimated the IWC using the H10 parameterization in this study. The H10 relationship was found to be valid for stratiform clouds over a wide range of temperatures and particle sizes over North China as well (Hou et al., 2021). Still, bias might be result from high ice particle concentrations.

3. Results and discussion

3.1. *The definition of in-cloud sample and the determination of cloud phase*

In previous aircraft observation studies, the definition of the in-cloud sample was based on the thresholds of N_c and/or LWC (Rangno and Hobbs, 2005; Noh et al., 2013; O'Shea et al., 2017; D'Alessandro et al., 2021; Huang et al., 2021). In our study, a 1-s in-cloud sample in MPTR was defined if either of the following two conditions was met: (1) M_{FCDP} was greater than 0.001 g m^{-3} or (2) the number concentration of particles larger than 50 μm from 2DS ($N_{2DS>50}$) was greater than 1 L^{-1}. The threshold of M_{FCDP} used in our study is similar to the studies listed above, which was found suitable in North China for in situ observation (Zhao et al., 2018). Also, the threshold of $N_{2DS>50}$ was used to determine the existence of large supercooled droplets and/or ice particles (D'Alessandro et al., 2021). Meanwhile, the altitude of the in-cloud sample had to be higher than 100 m above ground to remove the possible influence of fog or haze.

The cloud phase was determined from FCDP and 2DS separately after selecting the in-cloud samples and removing the noise (Fig. 2). Previous studies have suggested that the small particles from FCDP were usually liquid if the number concentration of FCDP (N_{FCDP}) was greater than 1 cm^{-3} (Lance et al., 2010; D'Alessandro et al., 2021). Therefore, the threshold value of $N_{FCDP} \geqslant 1$ cm^{-3} was used to determine whether the particles of FCDP were liquid in our study. When $N_{FCDP} \geqslant 1$ cm^{-3}, the phase of 2DS was determined using the "μ-method", which was similar to Korolev et al. (2003). In our study, we calculated the LWC and IWC of 2DS using the method in section 2.3, and μ equals the ratio of IWC to the sum of LWC_{2DS} and IWC. The phase of 2DS was regarded as ice if $N_{FCDP} \leqslant 1$ cm^{-3} since the absence of small supercooled droplets usually meant that there were no large supercooled droplets. The phase of each in-cloud sample was the combination of FCDP and 2DS (e.g., FCDP=liquid and 2DS=liquid were classified as liquid, FCDP=liquid and 2DS=mixed were classified as mixed, etc.). After determining the phase of the samples, we checked the 2DS images of the in-cloud samples. We found ice particles and/or liquid droplets for different cloud types, which suggested that the criterion for determining phase was suitable in our study.

Using this method, we have collected 69850 in-cloud 1-s samples in MPTR over the 22 flights mentioned in section 2.1. The detailed information regarding these flights is shown in Table 1, including the flight time, synoptic type, in-cloud samples in MPTR, temperature range of in-cloud samples, the fraction of ice, mixed-phase, and liquid clouds for each flight, and the air quality data. With the temperature decreasing, the number of in-cloud samples increased above –10°C and decreased at lower temperatures (Fig. 3). For all in-cloud samples in MPTR, the average fraction of liquid, mixed-phase, and ice cloud samples was 4.9%, 23.3%, and 71.8%, respectively. The relative fraction changed with temperature as well (Fig. 3). Ice fraction was larger than 30% at

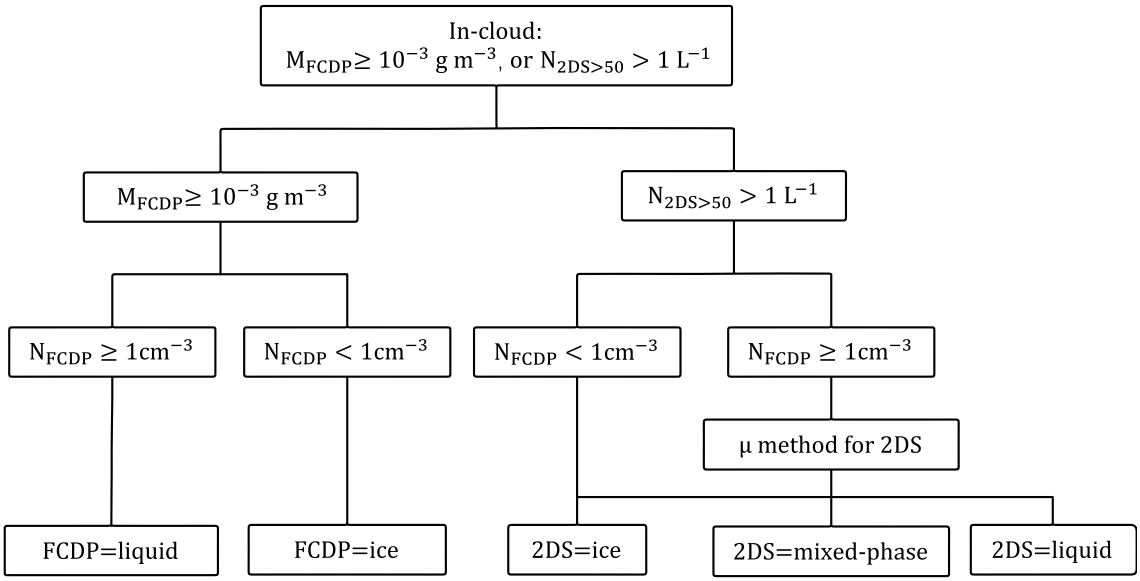

Fig. 2. Diagram of the cloud phase identification method used in this study.

all MPTR, reaching 90% below –30°C. Liquid and mixed fractions decreased with temperature decreasing, but liquid samples were still found at temperatures near −35°C. The fraction of different cloud types varied significantly from flight to flight, with the fraction of ice ranging from 5.3% to 99.2%, the fraction of mixed-phase ranging from 0.3% to 62.6%, and the fraction of liquid ranging from 0% to 91.3%. The difference can be attributed to the difference in sampling temperature between flights.

Figure 4 shows the probability density function (PDF) of the ice mass fraction (IMF), i.e., the ratio of IWC to total water content (TWC). Here, IWC and LWC were calculated by the method shown in Fig. 2, and TWC equaled the sum of IWC and LWC. Previous studies found a U-shaped distribution of IMF for cloud samples in MPTR (e.g., Korolev et al., 2003). Compared to the studies listed above, the probability of IMF < 0.1 was much smaller while the probability of IMF > 0.9 was much larger, making the U-shape become a half-U-shape. With the temperature decreasing, the probability of IMF < 0.1 decreased as well. The lower fraction of liquid cloud and the small probability of small IMF indicated that ice clouds dominated MPTR, while liquid clouds were rare in winter over north China. Because the mixed-phase clouds have a strong relationship with the rainfall and snowfall in winter, the discussion in the following sections is focused on mixed-phase clouds.

3.2. *The statistics of cloud microphysical properties for mixed-phase samples*

The statistical results of microphysical properties for mixed-phase samples, including N_c, LWC, N_i, IWC, TWC, the effective diameter of cloud droplets (D_c) and ice particles (D_i), are shown in Table 2, including the median values, the mean values, the standard deviations, and the coefficient of variations (CV, equaling to the ratio of standard deviation to mean). In our study, the effective diameter of both liquid droplets and ice particles was defined as the ratio of the third to the second moment of the PSDs.

For wintertime mixed-phase cloud samples, the average N_c and N_i were 43.9 ± 152.0 cm^{-3} and 42.3 ± 44.2 L^{-1}, respectively; the average LWC, IWC, and TWC were 0.032 ± 0.059, 0.136 ± 0.173, and 0.168 ± 0.193 g m^{-3}, respectively; the average D_c and D_i were 12.45 ± 7.24 μm and 436.61 ± 171.28 μm, respectively. The median values of cloud microphysical properties were smaller than the mean values, meaning that extremely large values existed in the datasets, indicating the complexity and variability of microphysical processes in mixed-phase clouds.

When comparing the CV of the microphysical properties (Table 2), we found that the CV of liquid-phase properties (N_c, LWC, and D_c) was larger than the corresponding ice-phase properties (N_i, IWC, and D_i), meaning that the liquid-phase properties were more variable. The larger CV for liquid properties differed from previous results (Gultepe et al., 2002; Lachlan-Cope et al., 2016), which found that CV for liquid properties was smaller than ice properties. But this is not surprising because the threshold of N_c (N_{FCDP}) in this study was smaller than those. The smaller threshold of N_c contained a large variation range of N_c, which represented the different development stages for mixed-phase clouds, from highly glaciated to highly supercooled. If we use $N_c \geq 10$ cm^{-3} as the threshold for liquid samples of FCDP, we would get a smaller CV for liquid properties (Table A1), which is more like the studies listed above.

The comparisons of cloud microphysical properties of wintertime mixed-phase cloud between this study and different mid-latitude regions are shown in Fig. 5, including the Southern Ocean (SO) [Ahn et al., 2017 (SO17); Wang et al., 2020 (SO20)], North America (NA) [Cober et al., 2001 (NA01); Fleishauer et al., 2002 (NA02)], and East Europe (EE) [Korolev et al., 2001 (EE01)]. Due to the differences in probes, the measurements of ice particles were different,

Table 1. The summary of meteorological conditions, flight information, and pollution index for the flights used in this study. The numbers in parentheses are the mean values (LST = UTC + 8).

Date	Time (LST)	Synoptic type (Upper air + surface)	In-cloud time in MPTR (s)	Temperature range (°C)	Ice (%)	Mixed (%)	Liquid (%)	AQI_ Beijing	PM2.5_ Beijing (μg m^{-3})
2014/02/28	1240–1610	Trough + high pressure	2744	–15.4– –1.0 (–11.2)	63.8	29.1	7.1	103	78
2015/01/14	1410–1640	Trough + high pressure	5350	–13.2– –0.7 (–12.0)	69.5	29.5	1.0	264	214
2015/01/25	1000–1230	Trough + high pressure	1046	–32.8– –3.0 (–25.3)	75.0	19.9	5.1	178	134
2015/11/05	1210–1630	Ridge + high pressure	6695	–36.3– –0.1 (–16.6)	79.4	19.2	1.4	144	110
2015/11/11	1308–1620	Weak trough + high pressure	407	–4.0– –0.1 (–2.0)	6.1	34.4	59.5	137	104
2015/11/17	1730–2020	Weak trough + high pressure	5153	–11.5– –3.2 (–9.8)	94.7	0.3	5.0	82	60
2016/01/16	0958–1145	Trough + easterly returning current	120	–20.3– –8.9 (–13.4)	8.3	43.3	48.4	162	123
2016/01/16	1820–2145	Trough + easterly returning current	6460	–39.8– –8.8 (–21.4)	63.2	35.4	1.4	162	123
2016/01/21	0730–0935	Weak trough + high pressure	367	–24.2– –7.0 (–14.3)	50.6	29.2	20.2	173	131
2016/11/29	1205–1545	Trough + high pressure	9841	–35.2– –5.7 (–21.4)	73.7	26.3	0	129	98
2016/12/12	1245–1620	Trough + high pressure	417	–12.3– –0.9 (–11.5)	99.2	0.8%	0	271	221
2017/02/07	0939–1156	Trough + high pressure	5872	–35.7– –1.2 (–19.2)	60.7	35.5	3.8	103	80
2017/11/24	1541–1818	Trough + low pressure	2652	–24.8– –3.9 (–23.2)	69.5	24.2	6.3	47	22
2020/01/05	1528–1718	Ridge + high pressure	2122	–25.5– –5.5 (–21.4)	95.1	0.2	4.7	83	61
2020/12/28	0954–1300	Weak trough + high pressure	3547	–39.8– –3.3 (–30.0)	98.9	0.4	0.7	77	56
2021/01/14	0938–1240	Trough + low pressure	2655	–36.4– –3.0 (–26.2)	66.4	27.3	6.4	80	53
2021/01/14	1600–1850	Trough + low pressure	1823	–39.8– –0.7 (–27.6)	97.2	1.8	1.0	80	53
2021/01/25	1038–1142	Trough + high pressure	2338	–12.6– –1.6 (–9.2)	75.4	22.9	1.7	176	133
2021/01/27	1538–1725	Trough + low pressure	4454	–24.0– –0.5 (–19.3)	37.2	62.6	0.2	55	26
2021/02/23	0958–1225	Trough + high pressure	3506	–39.8– –2.6 (–24.2)	95.5	3.5	1.0	49	28
2021/02/27	1614–1840	Ridge + high pressure	1452	–10.6– –3.5 (–9.9)	5.3	3.4	91.3	159	121
2021/02/28	1041–1228	Ridge + easterly returning current	829	–26.5– –0.1 (–8.3)	48.1	25.0	26.9	125	95
Total	–	–	69850	–39.8– –0.1 (–16.9)	71.8	23.3	4.9	–	–

while the measurements of liquid droplets were basically the same. As a result, we only compared the liquid-phase properties between different studies. However, the N_c thresholds of in-cloud samples differed in these studies, and some studies did not specify the thresholds of N_c. To better compare the difference, we used the results with the N_c threshold of 1 and 10 cm^{-3} (as shown in Table 2 and Table A1, respectively) for the comparison (the two different bars of "North China" in Fig. 5). The results with the N_c threshold of 10 cm^{-3} were a subset of our dataset. From Table 2 and Table A1, we found that the results were sensitive to the N_c thresholds, and the mean and median values of N_c and LWC became larger with larger N_c thresholds. Compared to the results of mixed-phase clouds from other mid-latitude regions, we found that N_c in our study was larger, while LWC and D_c were smaller. Though some studies (NA02 and SO20) did not provide D_c, we could estimate the range of D_c using formula (1) that D_c should be larger when N_c was smaller and LWC was larger. After this estimation, we found that the D_c of our research was smaller than these studies as well.

According to Martin et al. (1994), the width of the cloud droplet distribution (for droplets between 2 to 50 μm) could be described by parameter k, which is the ratio of the third power of mean volume diameter to the third power of the effective diameter. From this definition, smaller k usually

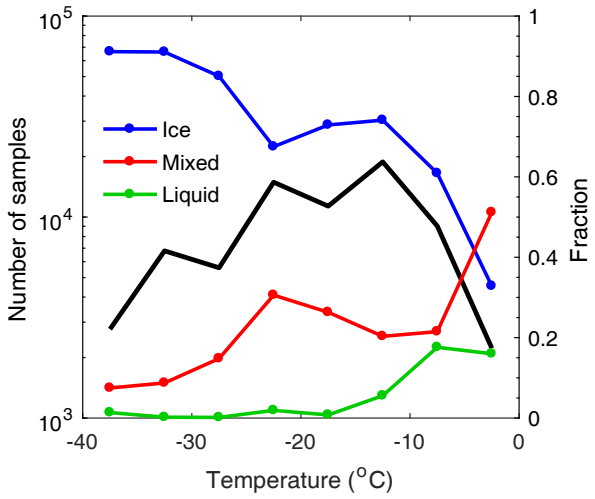

Fig. 3. The relationship between temperature and the number of in-cloud samples (black line) and the relative fraction of liquid (green line), mixed-phase (red line), and ice (blue line) samples.

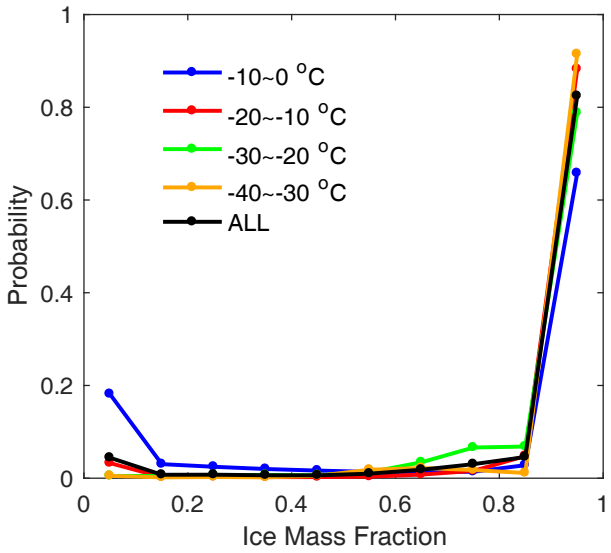

Fig. 4. The probability density function of ice mass fraction for different temperature intervals within the MPTR for all in-cloud samples.

Table 2. The statistical results regarding cloud microphysical properties for mixed-phase cloud samples.

Cloud Microphysical Properties	Median Value	Mean Value	Standard Deviations	Coefficient of Variation
N_c (cm^{-3})	1.8	43.9	152.0	3.45
LWC (g m^{-3})	0.015	0.032	0.059	1.85
D_c (μm)	10.35	12.45	7.24	0.58
N_i (L^{-1})	27.2	42.3	44.2	1.04
IWC (g m^{-3})	0.094	0.136	0.173	1.27
D_i (μm)	413.87	436.61	171.28	0.39
TWC (g m^{-3})	0.122	0.168	0.193	1.15

indicates broader droplet distributions. After calculation, we found that k was the smallest in this study, suggesting that the cloud droplet distribution was wider than in other regions (Table 3). Our small k was consistent with previous studies, which found that k for the continental or polluted clouds was smaller than maritime or clean clouds (Yum and Hudson, 2004).

The larger N_c and smaller D_c are consistent with the severe pollution caused by human activities in North China in winter (Liang et al., 2018). Since the observation of aerosols from aircraft was missing in most flights, we used the air quality data provided by the China National Environmental Monitoring Centre to verify the degree of pollution. The air quality index (AQI) was used to determine the polluted day if daily mean AQI > 100. We found that 13 of these 20 days for the flights were polluted days, and the average $PM_{2.5}$ for the 20 days was 97.4 μg m^{-3} in Beijing. This mass concentration was higher than the class 2 limit for the daily mean value and was much higher than the annual mean value in Beijing. Under severe pollution conditions, there existed an increase in N_c but a decrease in D_c compared to clean conditions, resulting in broader cloud droplet distribution. We found the larger values of N_c in different flights, which confirmed the common presence of large aerosol loading. The larger N_c and smaller D_c results are consistent with Jackson et al. (2012), suggesting that the clouds sampled in more polluted conditions had larger N_c but smaller D_c. The smaller LWC is consistent with the lower temperature during flights and the difference in air mass type. The average temperature in our study was lower than the other studies in comparison. Previous studies have found that LWC decreased slightly with temperature decreasing (Gultepe et al., 2002); thus, the LWC in our study was smaller. Besides, the LWC from continental studies (EE01, NA01, NA02, and this study) were also smaller than the maritime studies (SO17, SO20), which was same as the previous study about the difference in airmass type (Martin et al., 1994; Yum and Hudson, 2001).

3.3. *The cloud microphysical properties at different temperatures for mixed-phase samples*

It's essential to know how the statistical distributions of cloud microphysical properties vary with temperature, both for model simulation and remote sensing inversion. Since the different observation flights in our study were carried out at different altitudes and temperatures, we analyzed the relationship between temperature and cloud microphysical properties to obtain the statistical distributions. In our study,

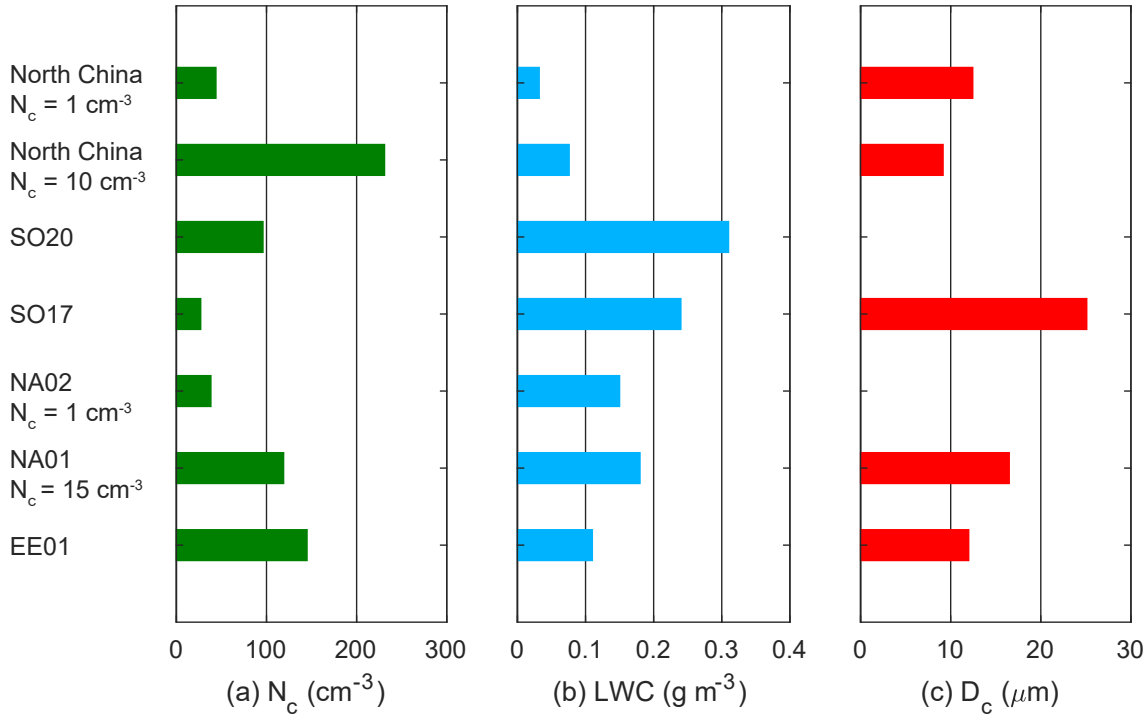

Fig. 5. The comparison of cloud microphysical properties (N_c, LWC, and D_c) of mixed-phase cloud samples between our study (North China) and previous studies (SO20: Wang et al., 2020; SO17: Ahn et al., 2017; NA02: Fleishauer et al., 2002; NA01: Cober et al., 2001; EE01: Korolev et al., 2001). The N_c thresholds for in-cloud samples are shown in the figure as well.

Table 3. The value of k for mixed-phase cloud samples in this study (North China) compared with previous studies (SO17: Ahn et al., 2017; NA01: Cober et al., 2001; EE01: Korolev et al., 2001).

Study	North China	SO17	EE01	NA01
k	0.56	0.66	0.69	0.64

the mixed-phase cloud samples appeared at all ranges of MPTR. Figure 6 shows box plots of mean values (red dots), median values (blue dots), 25th and 75th percentiles for N_c, LWC, D_c, N_i, IWC, and D_i. We averaged these properties into 2.5°C temperature bins for further analysis.

From Figs. 6a–c, it can be seen that N_c and LWC increase with increasing temperature, but the D_c decreases. The peak value of N_c appears at ~ –8°C, while the peak value of LWC appears at ~ –20°C. The range of variations of N_c and LWC in one temperature bin also increases when temperature increases. Still, the variation range of D_c in one temperature bin does not change much, and the outliers of D_c are less than N_c and LWC, which is consistent with the result that the CV of D_c is smaller than N_c and LWC. The increasing N_c and LWC with temperature increase is consistent with previous studies for wintertime mixed-phase cloud samples (Gultepe et al., 2002; Korolev et al., 2003; Noh et al., 2013).

From Figs. 6d–f, it can be seen that N_i decreases, but the D_i increases with temperature. In general, the larger values of N_i correspond to smaller D_i. What's more, with temperature increasing, the range of variation of N_i in one temperature bin decreases. In comparison, the variation range of D_i in one temperature bin increases, which is opposite to the liquid-phase properties. Unlike LWC, the IWC exhibited poor correlation with temperature, and the variation range in one temperature bin becomes larger when IWC is larger. The main reason for the poor correlation between IWC and temperature is the complicated ice-phase microphysical process (e.g., riming, aggregation, deposition, and WBF process) in mixed-phase clouds (Morrison et al., 2020). These microphysical processes could make ice particles more variable in shape and number at the same temperature, as the CV showed in Table 1. The decrease of N_i and the increase of D_i with increasing temperature are similar to previous studies for mixed-phase clouds in midlatitude regions (Fleishauer et al., 2002; Carey et al., 2008; Noh et al., 2013).

In conclusion, the statistical distributions of the variance of mixed-phase cloud microphysics with temperature are similar to other mid-latitude regions, although there exist some difference in statistical results of the cloud microphysical properties.

3.4. *The microphysical process at different temperatures for mixed-phase samples*

We next discuss the mixed-phase cloud samples at different temperatures. In order to better analyze the microphysical processes, the variation of PSDs and ice habits are discussed first. The whole dataset was divided into four intervals according to the cumulative distribution function (CDF) of tempera-

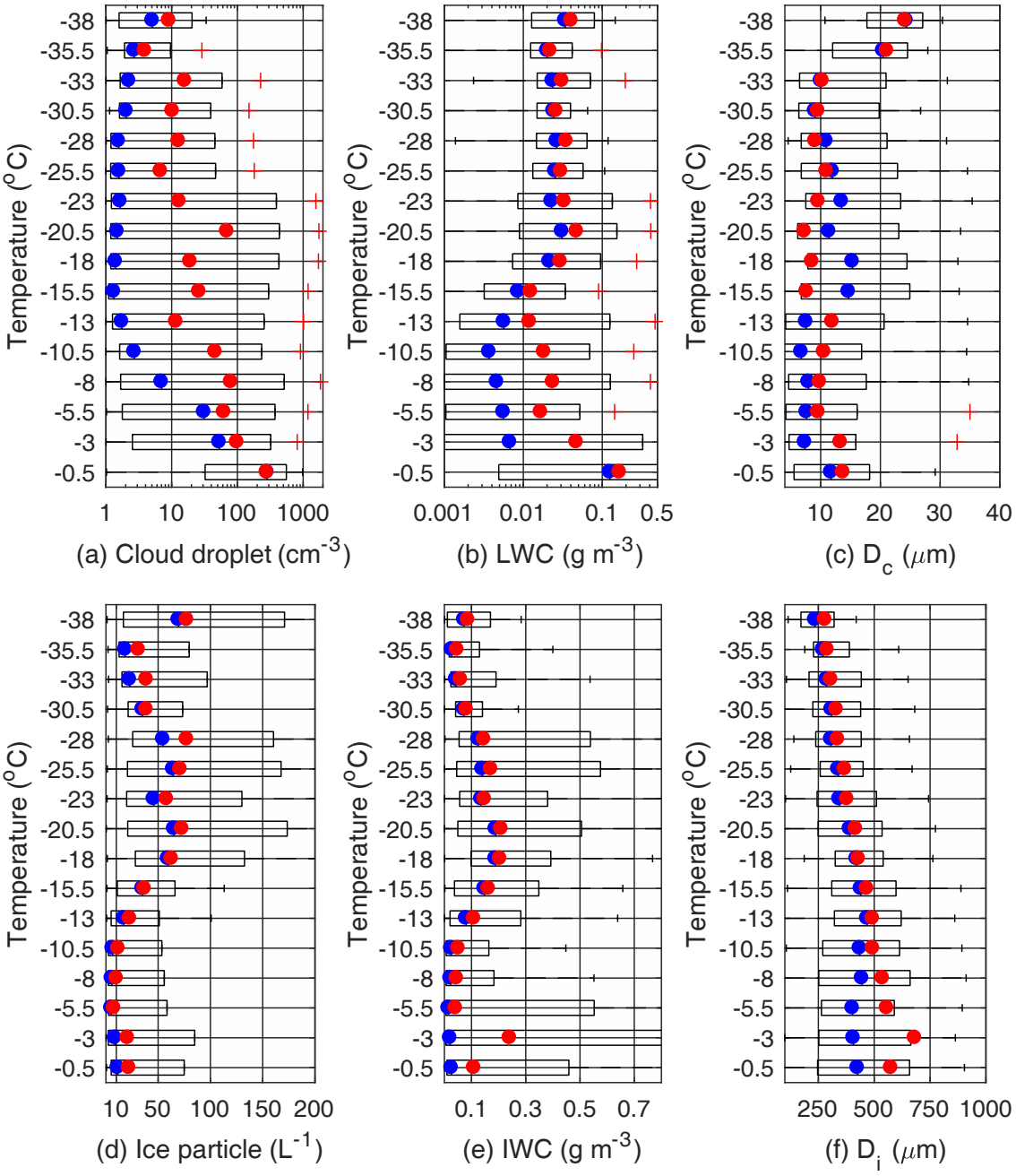

Fig. 6. Box plots as a function of temperature for (a) N_c, (b) LWC, (c) D_c, (d) N_i, (e) IWC, and (f) D_i for mixed-phase cloud samples. The red dots represented mean values; the blue dots represented median values; and the left and right sides of the box indicated the 25th and 75th percentiles, respectively. The whisker's length is 1.5IQR (IQR, the interquartile range, equal to the difference between 75th percentiles and 25th percentiles). The red crosses represented the outliers, which refer to a value more than 1.5IQR away from the bottom or top of the box.

ture: –10°C–0°C, –20°C– –10°C, –30°C– –20°C, and –40°C– –30°C. We calculated the average PSD and number concentration in each interval. Figure 7 shows the variation of PSDs for mixed-phase cloud samples at different temperature intervals.

The liquid PSDs are unimodal for different temperature intervals. As the temperature increases, the peaks of liquid PSDs remained unchanged (at around 5 μm), while the concentration of the peaks increases, which means there exist more small droplets at warmer temperatures. With the temperature rising, the number concentration of liquid droplets with diameters between 10 μm and 30 μm increases. The increase of small droplets with temperature is consistent with the N_c shown in Fig. 6a. Though the number concentration of liquid droplets with diameters larger than 100 μm decreases at higher temperatures, their existence still indicates the common presence of drizzle at different temperatures.

The ice PSDs are generally bimodal, but this feature

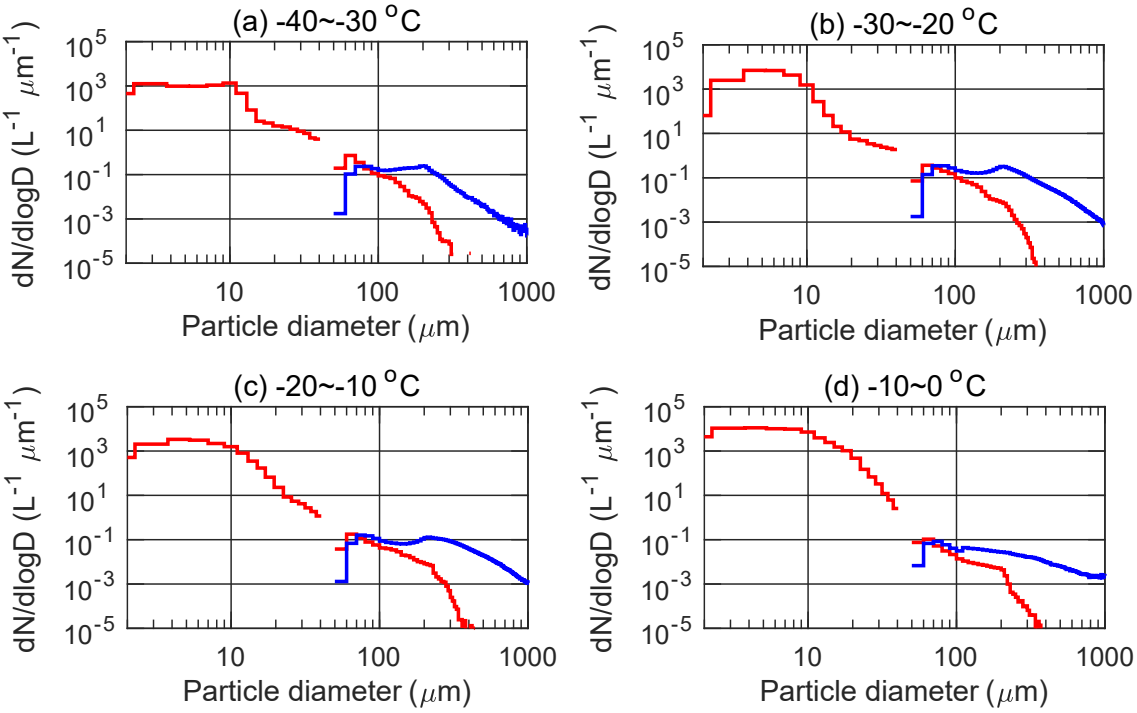

Fig. 7. The combined PSDs for mixed-phase cloud samples from FCDP and 2DS. The red lines are the average PSDs of liquid droplets, which combine the PSDs from FCDP and the liquid droplets from 2DS, and the blue lines are the average PSDs of ice particles from 2DS.

becomes less evident at higher temperatures. The ice PSDs exhibits the first peak at 80 μm. The peaks remain unchanged, but the number concentration of the peaks decreases as the temperature increases. The second peaks remain unchanged at around 200 μm, and the number concentration of these peaks decreases with temperature increasing. The decreasing of peaks of ice PSDs is consistent with the decreasing of N_i with temperature increasing, as shown in Fig.6d. The maximum diameter of the ice PSDs and the number concentration of ice particles with diameters larger than 600 μm become larger as the temperature increases. In comparison, the number concentration of ice particles smaller than 600 μm becomes smaller. Therefore, the D_i increases slightly with temperature increasing, as shown in Fig. 6f.

Images of hydrometeors of mixed-phase cloud samples from 2DS in different temperature intervals are shown in Fig. 8. These images were selected from different flights at the temperature intervals to be more representative. The coexistence of droplets and ice particles is found at all temperature intervals from the images of 2DS, though the droplets smaller than 10 μm cannot be recorded due to the resolution. Drizzle-sized drops are found at different temperatures, which confirms the inference in liquid PSDs. Though the supersaturation data was missing, we still found that the relationship between temperature and ice habit is basically the same as the habit diagram described by Bailey and Hallett (2009), i.e., we found that below –30°C (Fig. 8a), ice particles were mainly plates, columns, and column combinations, and the volume of ice particles was relatively small, and that with the temperature increasing, the ice particles become larger. What's more, larger irregular ice particles appear at higher temperatures (e.g., Figs. 8b, 8c, and 8d). Above –20°C, the ice particles were mostly plates, stellar crystals, irregular crystals, and capped columns (Figs. 8c and 8d), and the ice particles became larger. The aggregates of ice particles could be clearly observed above –10°C (e.g., Figs. 8d1, 8d2, and 8d3). The results of the ice particle size from 2DS images are consistent with the change of D_i shown in Fig. 6f.

The riming process refers to the growth of an ice particle by collision with supercooled cloud droplets. In contrast, the aggregation process clumps ice particles together to grow larger (Morrison et al., 2020). Previous studies have found that the aggregation and riming processes are two critical processes in mixed-phase clouds (Zhu et al., 2015; Lohmann et al., 2016; Taylor et al., 2016). From the analysis of the cloud properties, PSDs, and ice habits at different temperatures above, we could infer that the results are consistent with the operation of the aggregation and riming processes, and that the activity of these physical processes was different at different temperatures. We found that these two processes were not significant from the shape and number concentration of ice crystals at lower temperatures. As the temperature increased, the number concentration of liquid droplets larger than 100 μm reduced. This is consistent with the notion that large droplets were rimmed to ice particles, making the riming process more pronounced. At higher temperatures, especially above –10°C (e.g., Figs. 8d1, 8d2, and 8d3), there existed obvious aggregates of ice particles: D_i became larger while N_i became smaller, and more large ice particles

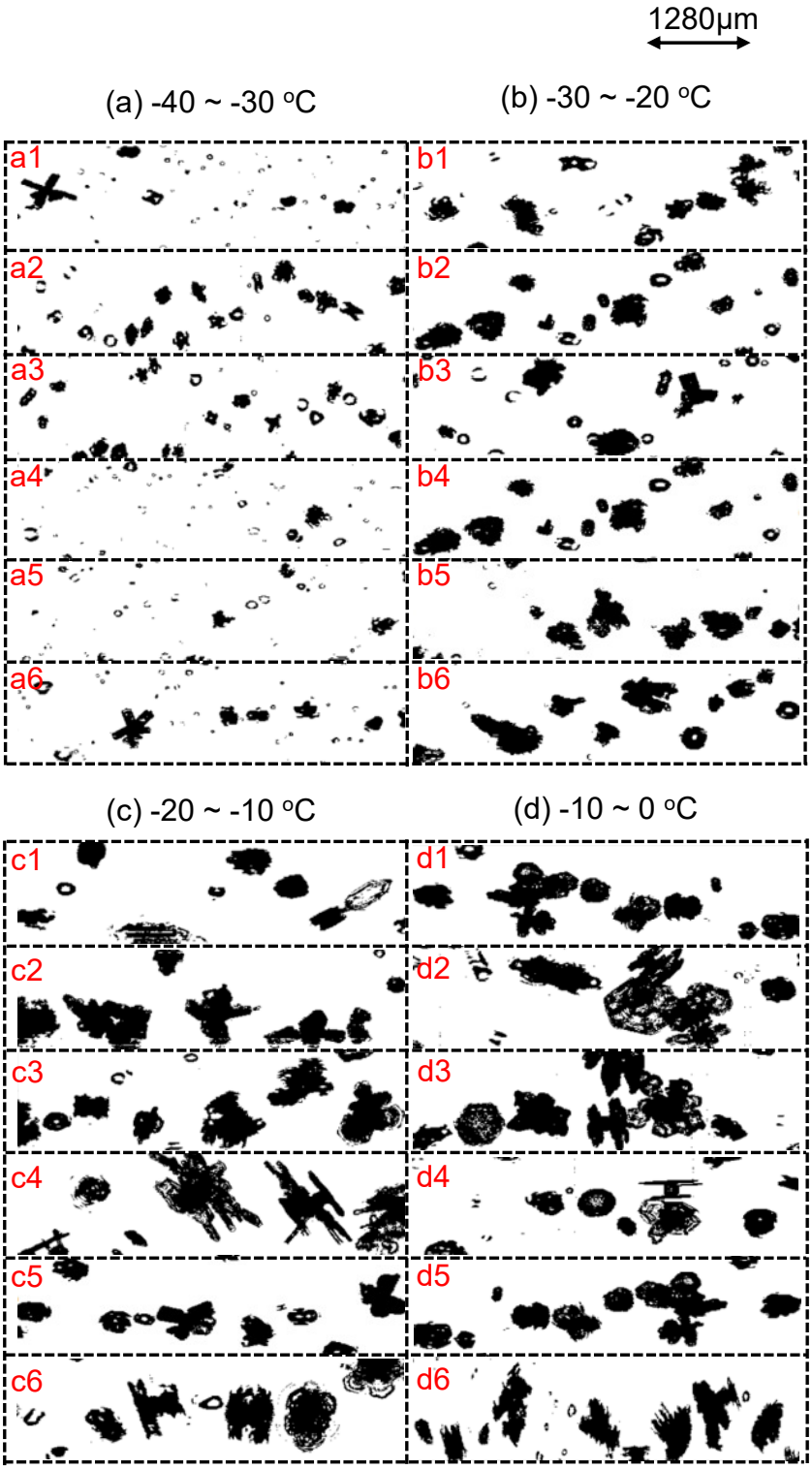

Fig. 8. Sampled images of mixed-phase cloud hydrometeor samples from 2DS under different temperature conditions. The images were selected from different flights in the corresponding temperature intervals, and the width of each 2DS channel is 1280 μm.

existed. This suggests that the larger particles came from the clumping of small ice particles. All these results are consistent with the aggregation process becoming more active at higher temperatures.

4. Summary

Using aircraft observational data, we investigated the statistics of the microphysical characteristics of wintertime

cold clouds in North China for the first time. The flights were carried out in winters from 2014 to 2017, 2020, and 2021, and the in-cloud data was 69,850 s in total.

For all in-cloud samples in mixed-phase temperature ranges (MPTR, –40°C to 0°C), the average fraction of liquid, mixed-phase, and ice cloud samples was 4.9%, 23.3%, and 71.8%. The ice fraction increases with decreasing temperature and reaches 90% below –30°C, while liquid and mixed fraction decrease. The probability of ice mass fraction (IMF) showed a "half-U-shape" with a small probability of IMF < 0.1 and a large probability of IMF > 0.9. This indicates that ice clouds dominated MPTR, while liquid clouds were rare in winter.

For wintertime mixed-phase cloud samples, the average N_c and N_i were 43.9 ± 152.0 cm^{-3} and 42.3 ± 44.2 L^{-1}, respectively; the average LWC, IWC, and TWC were 0.032 ± 0.059, 0.136 ± 0.173, and 0.168 ± 0.193 g m^{-3}, respectively; the average D_c and D_i were 12.45 ± 7.24 μm and 436.61 ± 171.28 μm, respectively. Compared to the observation for mixed-phase clouds results in winter in other mid-latitude regions, we found that N_c was larger while LWC and D_c were smaller in North China, resulting in the broader cloud droplet distribution. The larger N_c and smaller D_c are consistent with the existence of heavy pollution in winter in North China. The smaller LWC occurred during the lower temperature flights and change in air mass type.

The relationships between temperature and different cloud microphysical properties varied: N_c, LWC, and D_i increased as the temperature increased, but N_i and D_c decreased, and IWC exhibited a poor correlation with temperature. The relationship between temperature and cloud microphysical properties is similar to that found in previous studies in other mid-latitude regions, indicating that the temperature dependence of cloud microphysical properties was similar for mixed-phase clouds.

The liquid PSDs were unimodal, while the ice PSDs were bimodal. With increasing temperature, the peak of liquid PSDs remained unchanged, but the number concentration of the peaks increased. For ice PSDs, as the temperature increased, the first peaks remained unchanged, but the number concentration of these peaks decreased; the second peaks gradually shifted to larger sizes, and the number concentration of the peaks decreased.

The ice habit at different temperatures was basically the same as the description from Bailey and Hallett (2009). Ice particles were mainly plates and columns, with aggregates observed at lower temperatures, and small volumes of ice particles. At higher temperatures, the ice particles were mostly plates, stellar crystals, irregular crystals, and capped columns, and the particles became larger.

Our results are consistent with the operation of the aggregation and riming processes. The relative importance of these processes varied significantly at different temperatures, though both aggregation and riming processes were more active at higher temperatures.

This work fills the gap in the aircraft observation research of wintertime cold clouds in North China. This may also be helpful in the development of remote sensing retrieval algorithms and microphysical schemes in model simulations. The results suggested that ice clouds dominated MPTR, while liquid clouds were rare in winter in North China. Though the wintertime mixed-phase clouds had some unique microphysical characters in North China, the temperature dependence of cloud properties was basically consistent with previous results in other regions in winter. Besides, the dominant ice-phase microphysical processes in wintertime mixed-phase clouds were the aggregation and riming processes. However, due to the air traffic control and the risk of aircraft icing in winter, the flights of aircraft observations were fewer than in other seasons. The microphysical properties of wintertime cold clouds need to be thoroughly investigated under different weather conditions by aircraft observations in North China in the future. What's more, it is necessary to combine other observation methods such as satellite, lidar, and radar with aircraft observations to gain a more comprehensive understanding of the microphysical structure of these clouds.

Acknowledgements. This work is supported by the National Natural Science Foundation of China (Grant Nos. 41925023, 91744208, 41575073, 41621005, and 42075084) and by the Ministry of Science and Technology of the People's Republic of China (Grant Nos. 2017YFA0604002 and 2016YFC0200503). This research is also supported by the Collaborative Innovation Center of Climate Change, Jiangsu Province.

APPENDIX

Table A1. Same as Table 1, but the threshold for liquid phase of FCDP is 10 cm^{-3}.

Cloud Microphysical Properties	Median Value	Mean Value	Standard Deviations	Coefficient of Variation
N_c (cm^{-3})	130.8	231.0	288.6	1.25
LWC (g m^{-3})	0.038	0.076	0.114	1.51
D_c (μm)	8.31	9.16	3.74	0.41
N_i (L^{-1})	7.9	24.2	37.9	1.57
IWC (g m^{-3})	0.022	0.108	0.274	2.54
D_i (μm)	414.51	448.73	221.26	0.49
TWC (g m^{-3})	0.090	0.183	0.312	1.71

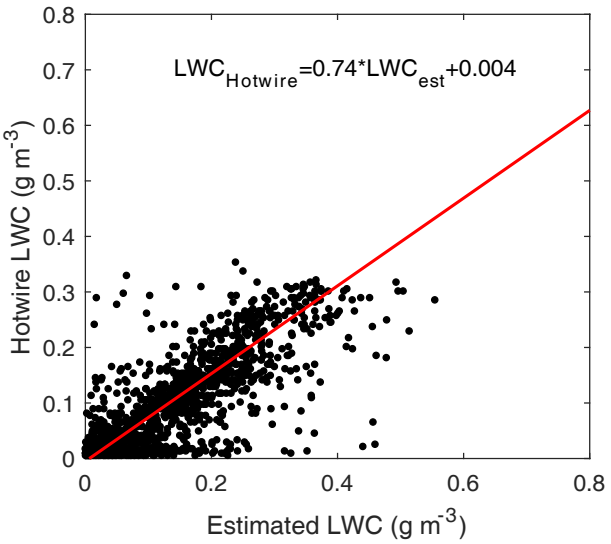

Fig. A1. Comparison between the Hotwire LWC ($LWC_{Hotwire}$) and estimated LWC (LWC_{est}, the sum of LWC from FCDP and 2DS) on the King Air 350 aircraft. The red line is the linear best fit line with a correlation coefficient of 0.88. The calibration was carried out by the Beijing Weather Modification Office staff in their laboratory.

REFERENCES

Ahn, E., Y. Huang, T. H. Chubb, D. Baumgardner, P. Isaac, M. de Hoog, S. T. Siems, and M. J. Manton, 2017: *In situ* observations of wintertime low-altitude clouds over the Southern Ocean. *Quart. J. Roy. Meteor. Soc.*, **143**, 1381–1394, https://doi.org/10.1002/qj.3011.

Ahn, E., Y. Huang, S. T. Siems, and M. J. Manton, 2018: A comparison of cloud microphysical properties derived from MODIS and CALIPSO with in situ measurements over the wintertime Southern Ocean. *J. Geophys. Res.*, **123**, 11 120--11 140, https://doi.org/10.1029/2018JD028535.

Bailey, M. P., and J. Hallett, 2009: A comprehensive habit diagram for atmospheric ice crystals: Confirmation from the laboratory, AIRS II, and other field studies. *J. Atmos. Sci.*, **66**, 2888–2899, https://doi.org/10.1175/2009JAS2883.1.

Baker, B., and R. P. Lawson, 2006: Improvement in determination of ice water content from two-dimensional particle imagery. Part I: Image-to-mass relationships. *J. Appl. Meteorol. Climatol.*, **45**, 1282–1290, https://doi.org/10.1175/JAM2398.1.

Brown, P. R. A., and P. N. Francis, 1995: Improved measurements of the ice water content in cirrus using a total-water probe. *J. Atmos. Oceanic Technol.*, **12**, 410–414, https://doi.org/10.1175/1520-0426(1995)012<0410:IMOTIW>2.0.CO;2.

Carey, L. D., J. G. Niu, P. Yang, J. A. Kankiewicz, V. E. Larson, and T. H. V. Haar, 2008: The vertical profile of liquid and ice water content in midlatitude mixed-phase altocumulus clouds. *J. Appl. Meteorol. Climatol.*, **47**, 2487–2495, https://doi.org/10.1175/2008JAMC1885.1.

Cober, S. G., G. A. Isaac, and J. W. Strapp, 2001: Characterizations of aircraft icing environments that include supercooled large drops. *J. Appl. Meteorol. Climatol.*, **40**, 1984–2002, https://doi.org/10.1175/1520-0450(2001)040<1984:COAIET>2.0.CO;2.

Crosier, J., and Coauthors, 2011: Observations of ice multiplication in a weakly convective cell embedded in supercooled mid-level stratus. *Atmospheric Chemistry and Physics*, **11**, 257–273, https://doi.org/10.5194/acp-11-257-2011.

D'Alessandro, J. J., G. M. McFarquhar, W. Wu, J. L. Stith, J. B. Jensen, and R. M. Rauber, 2021: Characterizing the occurrence and spatial heterogeneity of liquid, ice, and mixed phase low-level clouds over the southern ocean using in situ observations acquired during SOCRATES. *J. Geophys. Res.*, **126**, e2020JD034482, https://doi.org/10.1029/2020JD034482.

Faber, S., J. R. French, and R. Jackson, 2018: Laboratory and in-flight evaluation of measurement uncertainties from a commercial Cloud Droplet Probe (CDP). *Atmospheric Meas. Tech.*, **11**, 3645–3659, https://doi.org/10.5194/amt-11-3645-2018.

Fleishauer, R. P., V. E. Larson, and T. H. V. Haar, 2002: Observed microphysical structure of midlevel, mixed-phase clouds. *J. Atmos. Sci.*, **59**, 1779–1804, https://doi.org/10.1175/1520-0469(2002)059<1779:OMSOMM>2.0.CO;2.

French, J. R., and Coauthors, 2018: Precipitation formation from orographic cloud seeding. *Proc. Natl. Acad. Sci.*, **115**, 1168–1173, https://doi.org/10.1073/pnas.1716995115.

Friedrich, K., and Coauthors, 2020: Quantifying snowfall from orographic cloud seeding. *Proc. Natl. Acad. Sci.*, **117**, 5190–5195, https://doi.org/10.1073/pnas.1917204117.

Gultepe, I., and G. A. Isaac, 2004: Aircraft observations of cloud droplet number concentration: Implications for climate studies. *Quart. J. Roy. Meteor. Soc.*, **130**, 2377–2390, https://doi.org/10.1256/qj.03.120.

Gultepe, I., G. A. Isaac, and S. G. Cober, 2002: Cloud microphysical characteristics versus temperature for three Canadian field projects. *Ann. Geophys.*, **20**, 1891–1898, https://doi.org/10.5194/angeo-20-1891-2002.

Guo, X. L., D. H. Fu, X. Y. Li, Z. X. Hu, H. C. Lei, H. Xiao, and Y. C. Hong, 2015: Advances in cloud physics and weather modification in China. *Adv. Atmos. Sci.*, **32**, 230–249, https://doi.org/10.1007/s00376-014-0006-9.

Heymsfield, A. J., and J. L. Parrish, 1978: A computational technique for increasing the effective sampling volume of the PMS two-dimensional particle size spectrometer. *J. Appl. Meteorol. Climatol.*, **17**, 1566–1572, https://doi.org/10.1175/1520-0450(1978)017<1566:ACTFIT>2.0.CO;2.

Heymsfield, A. J., C. Schmitt, A. Bansemer, and C. H. Twohy, 2010: Improved representation of ice particle masses based on observations in natural clouds. *J. Atmos. Sci.*, **67**, 3303–3318, https://doi.org/10.1175/2010JAS3507.1.

Hou, T. J., H. C. Lei, Y. J. He, J. F. Yang, Z. Zhao, and Z. X. Hu, 2021: Aircraft measurements of the microphysical properties of stratiform clouds with embedded convection. *Adv. Atmos. Sci.*, **38**, 966–982, https://doi.org/10.1007/s00376-021-0287-8.

Hu, Y. X., S. Rodier, K.-M. Xu, W. B. Sun, J. P. Huang, B. Lin, P. W. Zhai, and D. Josset, 2010: Occurrence, liquid water content, and fraction of supercooled water clouds from combined CALIOP/IIR/MODIS measurements. *J. Geophys. Res.*, **115**, D00H34, https://doi.org/10.1029/2009JD012384.

Huang, Y., S. T. Siems, and M. J. Manton, 2021: Wintertime in situ cloud microphysical properties of mixed-phase clouds over the Southern Ocean. *J. Geophys. Res.*, **126**, e2021JD034832, https://doi.org/10.1029/2021JD034832.

Huo, J., Y. Tian, X. Wu, C. Han, B. Liu, Y. Bi, S. Duan, and D. Lyu, 2020: Properties of ice cloud over Beijing from surface Ka-band radar observations during 2014–2017. *Atmospheric Chem. Phys.*, **20**, 14 377–1 4392, https://doi.org/10.5194/acp-

20-14377-2020.

Jackson, R. C., and Coauthors, 2012: The dependence of ice microphysics on aerosol concentration in arctic mixed-phase stratus clouds during ISDAC and M-PACE. *J. Geophys. Res.*, **117**, D15207, https://doi.org/10.1029/2012JD017668.

Jensen, E. J., R. P. Lawson, J. W. Bergman, L. Pfister, T. P. Bui, and C. G. Schmitt, 2013: Physical processes controlling ice concentrations in synoptically forced, midlatitude cirrus. *J. Geophys. Res. Atmospheres*, **118**, 5348–5360, https://doi.org/10.1002/jgrd.50421.

Korolev, A., 2007a: Limitations of the Wegener–Bergeron–Findeisen mechanism in the evolution of mixed-phase clouds. *J. Atmos. Sci.*, **64**, 3372–3375, https://doi.org/10.1175/JAS4035.1.

Korolev, A., 2007b: Reconstruction of the sizes of spherical particles from their shadow images. Part I: Theoretical considerations. *J. Atmos. Oceanic Technol.*, **24**, 376–389, https://doi.org/10.1175/JTECH1980.1.

Korolev, A., J. W. Strapp, G. A. Isaac, and E. Emery, 2013: Improved airborne hot-wire measurements of ice water content in clouds. *J. Atmos. Oceanic Technol.*, **30**, 2121–2131, https://doi.org/10.1175/JTECH-D-13-00007.1.

Korolev, A., and Coauthors, 2017: Mixed-phase clouds: progress and challenges. *Meteor. Monogr.*, **58**, 5.1–5.50, https://doi.org/10.1175/AMSMONOGRAPHS-D-17-0001.1.

Korolev, A. V., G. A. Isaac, I. P. Mazin, and H. W. Barker, 2001: Microphysical properties of continental clouds from *in situ* measurements. *Quart. J. Roy. Meteor. Soc.*, **127**, 2117–2151, https://doi.org/10.1002/qj.49712757614.

Korolev, A. V., G. A. Isaac, S. G. Cober, J. W. Strapp, and J. Hallett, 2003: Microphysical characterization of mixed-phase clouds. *Quart. J. Roy. Meteor. Soc.*, **129**, 39–65, https://doi.org/10.1256/qj.01.204.

Korolev, A. V., E. F. Emery, J. W. Strapp, S. G. Cober, G. A. Isaac, M. Wasey, and D. Marcotte, 2011: Small Ice Particles in Tropospheric Clouds: Fact or Artifact? Airborne Icing Instrumentation Evaluation Experiment. *Bull. Am. Meteorol. Soc.*, **92**, 967–973, https://doi.org/10.1175/2010BAMS3141.1.

Lachlan-Cope, T., C. Listowski, and S. O'Shea, 2016: The microphysics of clouds over the Antarctic Peninsula - Part 1: Observations. *Atmospheric Chemistry and Physics*, **16**, 15 605–15 617, https://doi.org/10.5194/acp-16-15605-2016.

Lance, S., C. A. Brock, D. Rogers, and J. A. Gordon, 2010: Water droplet calibration of the Cloud Droplet Probe (CDP) and in-flight performance in liquid, ice and mixed-phase clouds during ARCPAC. *Atmospheric Measurement Techniques*, **3**, 1683–1706, https://doi.org/10.5194/amt-3-1683-2010.

Lawson, R. P., B. A. Baker, P. Zmarzly, D. O'Connor, Q. X. Mo, J.-F. Gayet, and V. Shcherbakov, 2006a: Microphysical and optical properties of atmospheric ice crystals at South Pole station. *J. Appl. Meteorol. Climatol.*, **45**, 1505–1524, https://doi.org/10.1175/JAM2421.1.

Lawson, R. P., D. O'Connor, P. Zmarzly, K. Weaver, B. Baker, Q. X. Mo, and H. Jonsson, 2006b: The 2D-S (stereo) probe: Design and preliminary tests of a new airborne, high-speed, high-resolution particle imaging probe. *J. Atmos. Oceanic Technol.*, **23**, 1462–1477, https://doi.org/10.1175/JTECH1927.1.

Liang, X., and Coauthors, 2018: SURF: Understanding and predicting urban convection and haze. *Bull. Amer. Meteor. Soc.*, **99**, 1391–1413, https://doi.org/10.1175/BAMS-D-16-0178.1.

Lloyd, G., and Coauthors, 2018: In situ measurements of cloud microphysical and aerosol properties during the break-up of stratocumulus cloud layers in cold air outbreaks over the North Atlantic. *Atmospheric Chemistry and Physics*, **18**, 17 191–17 206, https://doi.org/10.5194/acp-18-17191-2018.

Lohmann, U., J. Henneberger, O. Henneberg, J. P. Fugal, J. Bühl, and Z. A. Kanji, 2016: Persistence of orographic mixed-phase clouds. *Geophys. Res. Lett.*, **43**, 10 512–10 519, https://doi.org/10.1002/2016GL071036.

Ma, X. C., K. Bi, Y. B. Chen, Y. C. Chen, and Z. G. Cheng, 2017: Characteristics of winter clouds and precipitation over the mountains of northern Beijing. *Advances in Meteorology*, **2017**, 3536107, https://doi.org/10.1155/2017/3536107.

Martin, G. M., D. W. Johnson, and A. Spice, 1994: The measurement and parameterization of effective radius of droplets in warm stratocumulus clouds. *J. Atmos. Sci.*, **51**, 1823–1842, https://doi.org/10.1175/1520-0469(1994)051<1823:TMAPOE>2.0.CO;2.

Morrison, H., and Coauthors, 2020: Confronting the challenge of modeling cloud and precipitation microphysics. *Journal of Advances in Modeling Earth Systems*, **12**, e2019MS001689, https://doi.org/10.1029/2019MS001689.

Noh, Y.-J., C. J. Seaman, T. H. V. Haar, D. R. Hudak, and P. Rodriguez, 2011: Comparisons and analyses of aircraft and satellite observations for wintertime mixed-phase clouds. *J. Geophys. Res.*, **116**, D18207, https://doi.org/10.1029/2010JD015420.

Noh, Y.-J., C. J. Seaman, T. H. V. Haar, and G. S. Liu, 2013: In situ aircraft measurements of the vertical distribution of liquid and ice water content in midlatitude mixed-phase clouds. *J. Appl. Meteorol. Climatol.*, **52**, 269–279, https://doi.org/10.1175/JAMC-D-11-0202.1.

O'Shea, S. J., and Coauthors, 2017: In situ measurements of cloud microphysics and aerosol over coastal Antarctica during the MAC campaign. *Atmospheric Chemistry and Physics*, **17**, 13 049–13 070, https://doi.org/10.5194/acp-17-13049-2017.

Plummer, D. M., G. M. McFarquhar, R. M. Rauber, B. F. Jewett, and D. C. Leon, 2014: Structure and statistical analysis of the microphysical properties of generating cells in the comma head region of continental winter cyclones. *J. Atmos. Sci.*, **71**, 4181–4203, https://doi.org/10.1175/JAS-D-14-0100.1.

Quan, J. N., and X. C. Jia, 2020: Review of aircraft measurements over China: Aerosol, atmospheric photochemistry, and cloud. *Atmospheric Research*, **243**, 104972, https://doi.org/10.1016/j.atmosres.2020.104972.

Rangno, A. L., and P. V. Hobbs, 2005: Microstructures and precipitation development in cumulus and small cumulonimbus clouds over the warm pool of the tropical Pacific Ocean. *Quart. J. Roy. Meteor.. Soc.*, **131**, 639–673, https://doi.org/10.1256/qj.04.13.

Storelvmo, T., 2017: Aerosol effects on climate via mixed-phase and ice clouds. *Annual Review of Earth and Planetary Sciences*, **45**, 199–222, https://doi.org/10.1146/annurev-earth-060115-012240.

Taylor, J. W., and Coauthors, 2016: Observations of cloud microphysics and ice formation during COPE. *Atmospheric Chemistry and Physics*, **16**, 799–826, https://doi.org/10.5194/acp-16-799-2016.

Wang, J. Y., X. Q. Dong, and B. K. Xi, 2015: Investigation of ice cloud microphysical properties of DCSs using aircraft in situ

measurements during MC3E over the ARM SGP site. *J. Geophys. Res.*, **120**, 3533–3552, https://doi.org/10.1002/2014JD022795.

Wang, Y., and Coauthors, 2020: Microphysical properties of generating cells over the Southern Ocean: Results from SOCRATES. *J. Geophys. Res.*, **125**, e2019JD032237, https://doi.org/10.1029/2019JD032237.

Yang, J. F., and H. C. Lei, 2016: In situ observations of snow particle size distributions over a cold frontal rainband within an extratropical cyclone. *Asia-Pacific Journal of Atmospheric Sciences*, **52**, 51–62, https://doi.org/10.1007/s13143-015-0089-y.

Young, G., and Coauthors, 2016: Observed microphysical changes in Arctic mixed-phase clouds when transitioning from sea ice to open ocean. *Atmospheric Chemistry and Physics*, **16**, 13 945–13 967, https://doi.org/10.5194/acp-16-13945-2016.

Yum, S. S., and J. G. Hudson, 2001: Microphysical relationships in warm clouds. *Atmospheric Research*, **57**, 81–104, https://doi.org/10.1016/S0169-8095(00)00099-5.

Yum, S. S., and J. G. Hudson, 2004: Wintertime/summertime contrasts of cloud condensation nuclei and cloud microphysics over the Southern Ocean. *J. Geophys. Res.*, **109**, D06204, https://doi.org/10.1029/2003JD003864.

Zhao, C. F., Y. M. Qiu, X. B. Dong, Z. E. Wang, Y. R. Peng, B. D. Li, Z. H. Wu, and Y. Wang, 2018: Negative aerosol-cloud r_e relationship from aircraft observations over Hebei, China. *Earth and Space Science*, **5**, 19–29, https://doi.org/10.1002/2017EA000346.

Zhao, Z., and H. C. Lei, 2014: Aircraft observations of liquid and ice in midlatitude mixed-phase clouds. *Adv. Atmos. Sci.*, **31**, 604–610, https://doi.org/10.1007/s00376-013-3083-2.

Zhu, S. C., X. L. Guo, G. X. Lu, and L. J. Guo, 2015: Ice crystal habits and growth processes in stratiform clouds with embedded convection examined through aircraft observation in Northern China. *J. Atmos. Sci.*, **72**, 2011–2032, https://doi.org/10.1175/JAS-D-14-0194.1.